Chemical Engineering Journal 148 (2009) 191–200

Contents lists available at ScienceDirect

Chemical Engineering Journal

journal homepage: www.elsevier.com/locate/cej

AISI 304 Austenitic stainless steels monoliths for catalytic applications

L.M. Martínez T*, O. Sanz, M.I. Domínguez, M.A. Centeno, J.A. Odriozola

Departamento de Química Inorgánica e Instituto de Ciencia de Materiales de Sevilla, Universidad de Sevilla-CSIC, Avda. Américo Vespucio 49, 41092 Sevilla, Spain

ARTICLE INFO

Article history:
Received 15 September 2008
Received in revised form
28 November 2008
Accepted 17 December 2008

Keywords:
Metallic monolith
Austenitic stainless steel
Gold catalysts
CO oxidation

ABSTRACT

The thermal treatments of austenitic stainless steels monoliths were studied in order to generate a highly homogeneous and rough oxide scale strongly attached to the base alloy, which will subsequently ensure the good adherence of the catalysts. In this work it has been shown that the morphology, integrity and homogeneity of the scale are strongly influenced by the temperature and time of treatment. Washcoating method was used to deposit on the monolith surface a Au/CeO_2 catalyst. The drying procedure turned out to be the most critical variable for the adherence and homogeneity of the catalytic ceria layer, while the ceria colloid concentrations in the starting aqueous dispersion seems to have only a threshold effect. The monolithic reactors containing Au/CeO_2 layers are active in the oxidation of CO.

1. Introduction

Monolithic supports are uni-body structures composed of parallel repeating cells or channels. Nowadays, there are an increasing demand for the development and evaluation of the monoliths for many reactor applications, e.g. chemical process and refining industries, catalytic combustion and ozone abatement among others [1–15]. Monoliths are made of ceramic or metallic materials, these presenting a series of comparative advantages with respect to ceramic ones, i.e., higher mechanical resistance and thermal conductivity, and better prospects for achieving high cell densities [10]. Nevertheless, the preparation of catalytic devices based on metallic monoliths has a critical point, the adhesion of the catalytic layer to the metallic substrate.

For manufacturing metallic monoliths different metals and alloys have been proposed searching optimized mechanical properties, chemical and thermal stability as well as thin foil availability. Typically, Al-alloyed ferritic stainless steels are mostly used since high temperature oxidation produces alumina scales that improve the adhesion of the catalytic layer to the monolith [1,2,7,10]. The use of austenitic stainless steels as metallic support for catalytic devices has been demonstrated, particularly for reactions in which the carbon activity is low at moderate temperatures [12,14]. Similarly, when the working temperature is low, as in the catalytic combustion of volatile organic compounds, aluminium may be used. The excellent mechanical and thermal properties of this material, and the easiness for producing high surface area alumina layers with tailored porosity makes this alloy very attractive for building metallic monoliths [3,8,15]. Austenitic stainless steels develop at high temperatures, under oxidizing conditions, a protective chromia scale responsible for the durability and corrosion resistance of these particular alloys [16]. The nature of the compounds forming the scale depends on the alloying elements as well as on the temperature, time and atmosphere composition [16–19]. These elements determine whether the preferential oxidation of the elements that constitute the alloy results in the development of a resistant, rough and homogeneous scale to improve the anchoring of the catalytic phase to the substrate [16,19]. The nature of the catalytic layer may also affect the scale adhesion and corrosion resistance since it has been demonstrated that the addition of the so-called reactive elements enhances these properties, among the reactive elements lanthanum and cerium are widely used either as surface addition [19–24] or as microalloying element [25]. The use of reactive elements solutions acting as a primer on the surface of microchannel catalytic reactors for the steam reforming of methane has been also patented [24]. In previous works, our group has demonstrated that cerium deposited on top of stainless steels migrates to the alloy/scale interface independently the way of deposition: pyrolisis of aerosols, ion implantation or immersion in cerium nitrate solutions [20,21,23]. Therefore, the nature of the oxide scale may affect the catalytic properties of the monolith since the elements present in the alloy scale, manganese, iron and chromium oxides, may present catalytic properties by themselves or in conjunction with the deposited catalytic layer while the physical properties of the scale might be affected by the presence of the catalytic layer containing reactive elements as cerium.

The aim of this work is to study the preparation variables for obtaining well adhered catalytic ceria layers on structured catalytic reactors built from austenitic stainless steel. The study is focused on the preparation and characterization of AISI 304 stainless

* Corresponding author.
E-mail address: leidy@icmse.csic.es (L.M. Martínez T).

1385-8947/$ – see front matter © 2008 Elsevier B.V. All rights reserved.
doi:10.1016/j.cej.2008.12.030

Table 1
Composition of the commercial EN-1.4301 stainless steel sheet used (Fe balance).

Element	Cr	Ni	Si	Mn	N	C	Cu	Mo	P	S	Co	V	W
wt.%	18.4	8.11	0.44	1.45	0.057	0.064	0.23	0.25	0.03	0.001	0.2	0.13	0.15

steel monoliths washcoated with Au/CeO_2 catalyst. As a result of this work we will propose thermal treatments and washcoating procedures resulting in AISI 304 monoliths mechanically stable washcoating and active in the CO oxidation reaction.

2. Experimental

2.1. Preparation of the structured support

A commercial EN-1.4301 austenitic stainless steel sheet (50 μm thick) was used as raw material. Table 1 shows a typical compositional analysis. Monoliths were prepared by rolling around a spindle alternate flat (160 mm × 30 mm) and corrugated (220 mm × 30 mm) sheets [10]. The final monolith is a cylinder of 30 mm height, 16 mm diameter and a cell density of 55 cell cm^{-2} (Fig. 1).

Thermal treatments were used for generating a rough and adherent oxide scale adequate to further washcoating of the catalyst.

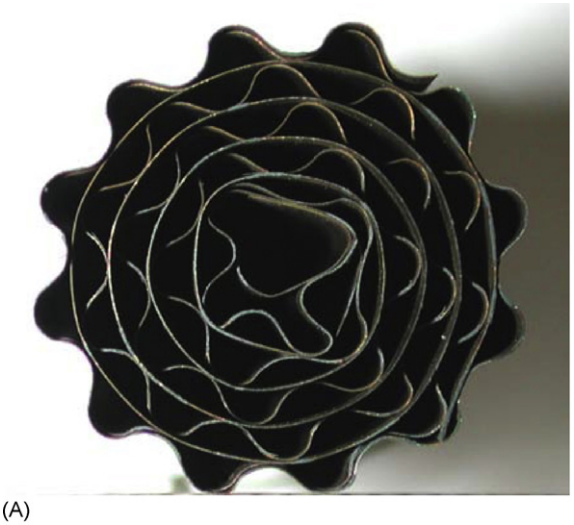

(A)

(B)

Fig. 1. Channels of corrugated AISI 304 austenitic stainless steel monolith.

Prior to any treatment the steel sheets were washed with water and soap, cleaned with water and then carefully rinsed with acetone to remove the organic impurities. Monoliths were oxidized in batches of three in an 1100 W horizontal furnace. Using a 10 ml min^{-1} flow of synthetic air from room temperature to the target temperature (875–925 °C) at 10 °C min^{-1}, maintained for the scheduled time at the target temperature (30–120 min) and then cooled down to room temperature under the same atmosphere. These treatments will allow the optimization of the main physicochemical characteristics of the generated oxide layer and the development of the procedure that creates the most homogeneous and resistant scale.

2.2. Catalyst coating deposition over the monoliths

2.2.1. CeO_2 deposition

A commercial CeO_2 colloid (Nyacol) which properties are described in Table 2 was used for preparing the different slurries. In order to optimize the rheological properties of the colloidal solutions, to improve the homogeneity of the catalytic deposit and to avoid cracking effects of the layer, the initial concentration of solids in the colloidal solutions was investigated by modifying the solids content between 2 and 20 wt.%. The colloidal suspensions were prepared by adding the adequate amount of double distilled water to the commercial colloid. The thermally pretreated monoliths were immersed into the colloidal suspension for coating for 1 min and then withdrawn at a constant speed of 3 cm h^{-1}. To avoid the obstruction of monoliths channels, the excess of colloid was removed by centrifugation at 400 rpm for 10 min. After the catalytic layer deposition the monoliths were dried and subsequent calcination has to be performed for a complete elimination of water and counter ions from the colloid suspension. The drying procedure may result in cracking and spalling of the catalytic layer which depends strongly on the wetting properties of the colloidal suspension. In order to study this effect the monoliths were either oven-dried or freeze-dried according to the following procedures:

- The monoliths were oven-dried at 80 °C for 3 h cooled down, and then the temperature was increased up to 500 °C with a constant rate of 2 °C min^{-1} in static air. This temperature is maintained for 4 h and the monolith was cooled down to room temperature.
- The monoliths were dried as described above but the calcination procedure starts at 80 °C once the drying step is finished.
- The monoliths were freeze-dried for 2 or 4 h and once the temperature increase to the room temperature are calcined at 500 °C for 4 h as described above.

To increase the amount of the catalysts loading on the monoliths the procedures were repeated and successive coating, drying and calcination were carried out.

Table 2
Typical properties of the CeO_2 colloid.

CeO_2 (wt.%)	20
Solvent	Water
Particle size (nm)	10–20
Particle charge	+
pH	3.0
Specific gravity (g cm^{-3})	1.22
Viscosity (cP)	10
Counter ion (mol/mol)	0.4 acetate

2.3. Catalytic activity

The catalytic oxidation of CO was performed in a conventional continuous flow U-shaped glass reactor working at atmospheric pressure. The composition of the inlet and outlet gases was analysed with a Balzers Omnistar Bentchtop mass spectrometer with capabilities for quantitative analysis. The light-off curves for CO oxidation (500 °C, 5 °C min^{-1}) were obtained with a gas mixture containing 3.4% CO and 21% O_2 balanced by He at a total flow rate of 42 ml min^{-1}. A blank reaction with an empty reactor, in the absence of metallic monolith, showed no activity under these conditions. The catalytic devices were pre-activated "in situ" at 500 °C for 60 min (79% N_2 and 21% O_2).

2.4. Characterization

X-ray diffraction (XRD) analysis was performed on a Siemens diffractometer D500. Diffraction patterns were recorded using Cu-Kα radiation (λ = 1.5404 Å) over a 20–80° 2θ-range and a position-sensitive detector with 0.05° step size at a scan rate of 3° min^{-1}.

SEM-EDX allows the study of the morphology and element distribution profiles of the samples. A JEOL 5400 instrument equipped with an Energy Dispersive X-ray Spectrometer (OXFORD LINK TETRA 1128–231) was used.

X-ray photoelectron spectroscopy (XPS) analysis was carried out in an ultra-high vacuum chamber (UHV) to which an energy electron analyser (VG 100 AX) was fitted (vacuum better than 1×10^{-9} Torr, Al-Kα radiation, 15 kV, 20 mA). Before analysis, the samples were degassed under vacuum (10^{-7} Torr) in the pre-treatment chamber and then introduced in the analysis chamber. After subtraction of a Shirley-type nonlinear baseline, the spectra were decomposed according to a commercial fitting program (VGX 900) with a Gaussian/Lorentzian ratio of 85/15. Binding energies are referenced to the spurious C (1s) signal at 284.6 eV. The atomic ratios were calculated from relative intensities corrected by the Scofield factor of each atom.

The adherence of the scale and the catalytic layer to the substrate was evaluated using the ultrasonic method previously described [26]. It consists in the measurement of the weight loss caused by the exposition of the sample to ultrasound. The monoliths immersed in acetone were submitted to an ultrasonic treatment in a Cole Parmer ultrasonic bath (47 kHz and 130 W) for 60 min at room temperature. After that, the samples were dried and calcined. The weight loss was determined by the difference in the mass of the samples before and after the ultrasonic test. The results are presented in terms of adherence in the Table 3, where the adherence is the retained quantity on the monolith expressed in percentage.

Roughness was measured with a Mitutoyo SJ-201P surface roughness tester.

The textural properties were studied by N_2 adsorption–desorption measurements at liquid nitrogen temperature in Micromeritics ASAP 2020 apparatus between 0.1 and 0.995 mmHg with a homemade cell that allows analysing the complete monolith. Before analysis, the monoliths were degassed for 2 h at 423K in vacuum.

In-depth compositional analysis of both the oxide scale and the catalytic layer were determined by Glow Discharge Optical Emission Spectroscopy (GD-OES) experiments using a LECO GDS 750A spectrometer. The GD-OES analyses were performed with a Grimm lamp in the DC mode at 700 V using a constant power of 14 W. In every case a 4 mm area was analysed ensuring average macroscopic information of the analysed layers.

3. Results and discussion

3.1. Structural support pre-treatment

The influence of the oxidation conditions, time and temperature, on the weight gain and physical properties of the oxidized layer is presented in Table 3. The weight gain and scale thickness increases with the increase of the temperature at a constant oxidation time (60 min) (Table 3). Nevertheless, surface roughness shows a maximum for the sample treated at 900 °C, and the same behaviour is observed for the adherence (Fig. 2A). Despite the excellent adherence value for the sample treated at 925 °C the existence of blisters on the surface is clearly observed. These blisters are produced during the cooling due to the different thermal expansion coefficients between the oxide scale and the base metal. The mechanical integrity of the oxide layer is influenced by the thermal stress among all the other factors [22,27]. This arises as a result of the mismatch between thermal expansion coefficients of the oxide layer and the metal, being the oxide coefficient lower for all relevant temperatures. This stress may result in scale cracking and further spalling. The influence of the oxidation time on the weight gain and physical properties of the oxidized layer is studied at fixed oxidation temperature of 900 °C. The weight gain and the scale thickness increase when increasing the oxidation time. Initially, the scale grows through a solid-state diffusion mechanism depending on the growth rate of the scale thickness as early proposed by Wagner [16]. As the oxidation time increases, up to 75 min, the growth rate decreases following a parabolic behaviour (Fig. 2B). For the times higher than 75 min a dramatic weight gain occurs and after that the oxidation kinetics follows more or less a parabolic law (Fig. 2B). Thus, a maximum in the scale roughness and adherence can be observed for 60 min oxidation time while the formation of blisters was still absent (Table 3). This phenomenon can be associated with the cracking and spalling of the formed scale. For thicknesses above a critical value the mechanical stresses

Table 3
Properties of the oxidation layer for different thermal treatments conditions for AISI 304 ferritic stainless steel.

Temperature (°C)	Time (min)	Gain weight (mg)	Thickness (μm)[a]	Roughness (μm)[b]	Surface morphology[c]	Blister formation[c]	Adherence (%)
875	60	23.8	0.52	0.49	Heterogeneous	X	99.2
900	60	25.9	0.72	1.35	Homogeneous	X	99.6
925	60	54.8	1.18	0.82	Heterogeneous	√	97.3
900	30	9.2	0.25	0.68	Heterogeneous	X	99.0
900	60	25.9	0.72	1.35	Homogeneous	X	99.6
900	75	29.8	0.84	1.30	Heterogeneous	√	99.3
900	90	56.7	1.11	1.31	Heterogeneous	√	97.9
900	105	65.1	1.70	0.90	Heterogeneous	√	97.6
900	120	70.1	1.91	0.99	Heterogeneous	√	96.9

[a] GD-OES data.
[b] Roughness of the base alloy = 0.4 μm.
[c] From SEM image.

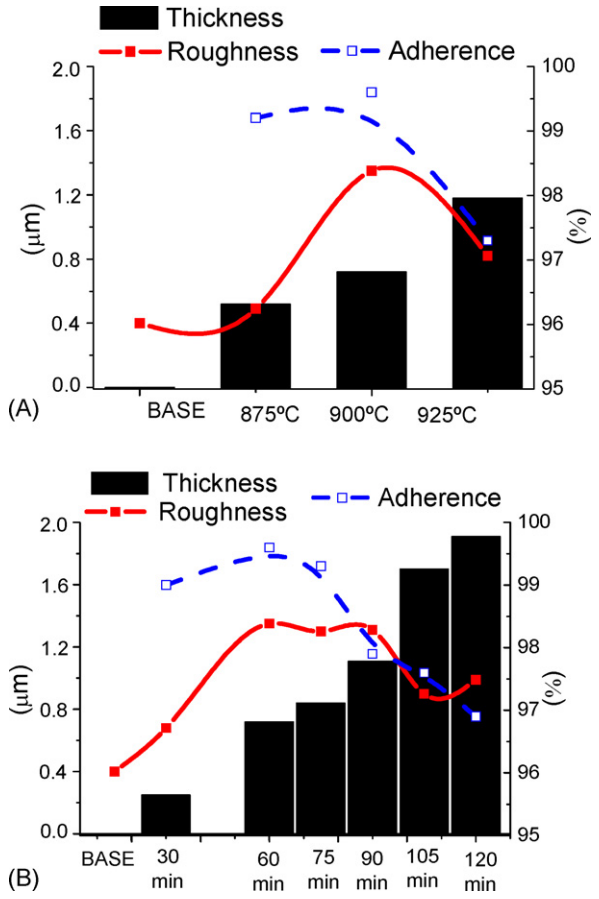

Fig. 2. Roughness values of monolith at different treatment conditions. (A) Fixed temperature in 900 °C and (B) fixed time in 60 min.

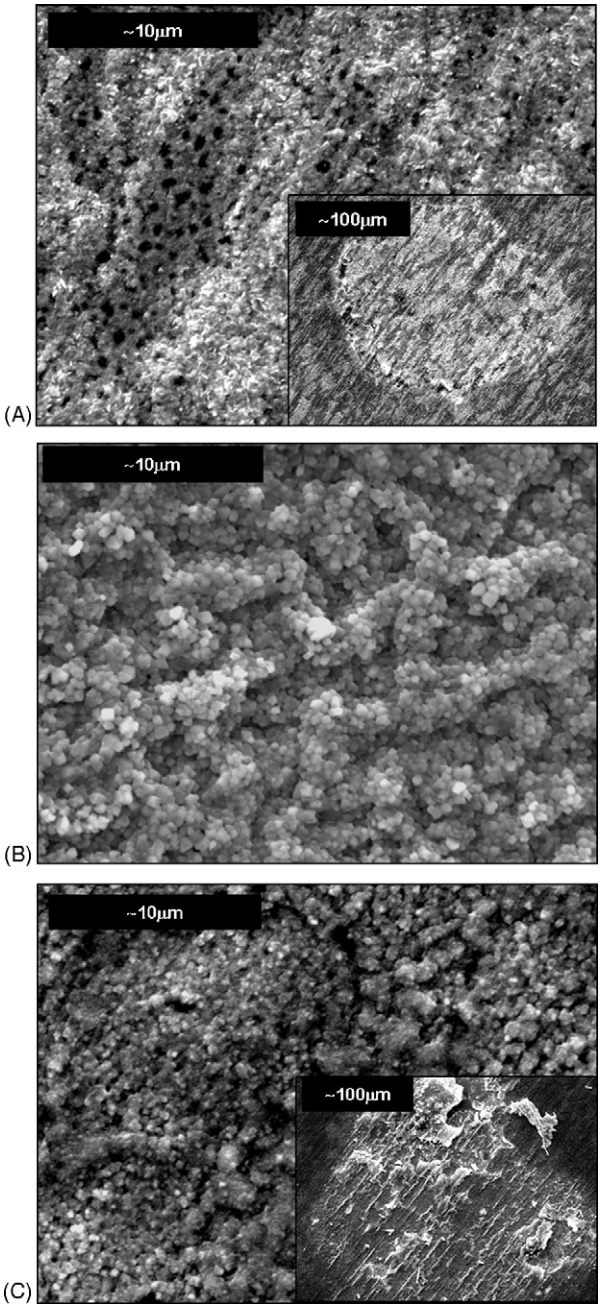

Fig. 3. SEM micrograph. of the top view of AISI 304 austenitic stainless steel foil, treated at different temperature for 60 min: (A) 875 °C, (B) 900 °C and (C) 925 °C.

associated with the differences in thermal expansion coefficients between the alloy and the oxide scale results in cracking and spalling of the oxide scale which causes an increase of the oxidation rate due to the existence of nude metal but as the time increase the parabolic behaviour is recovered [22]. The adherence value shows a maximum for 60 min oxidation and confirms that the waving value for the roughness are in accordance with the cracking and spalling behaviour of the oxide scale as a function of time.

The homogeneity of the surface and the formation of blisters can be observed through SEM images. For the highest temperature the formation of blisters and spalled areas are clearly seen in Fig. 3C, on the contrary for the lowest temperature tried in this study the surface is not homogeneous (Fig. 3A). The oxide scale did not cover completely the metallic surface. The sample oxidized 60 min at 900 °C in synthetic air shows a rather homogeneous aspect with the surface covered by small octahedral crystals randomly oriented (Fig. 3B). Insets a–c in Fig. 4 show a selection of SEM images of the oxidized monolith surface at 900 °C as a function of time. For short oxidation times the oxide scale is not homogeneous enough and the grain boundaries can still be observed but if the oxidation times increased above 60 min the existence of Fe-rich blisters are clearly present causing cracking and spalling of the oxide scale.

The oxide scale was characterized by XRD and are presented as a function of oxidation time and temperature in Fig. 5. The base alloy presents the characteristic diffraction lines of the fcc structure of the alloy ($2\theta = 43.7°$, 51.2° and 74.5°), as shown in Fig. 5A. Together with these diffraction lines, signals corresponding to the spinel structure $M'M_2O_4$ ($M' = M = Mn$, Fe, Cr) and α-M_2O_3 (M = Cr, Fe) are observed whatever the oxidation temperature or the oxidation time is. Detailed analysis of the phase formation as a function of time and temperature could be found elsewhere [19–23]. Besides this, it is worth to mention that the intensity of the Bragg peak corresponding to the austenite phase (fcc) changes with the treatment parameters: temperature and time. The intensity of these Bragg peaks decreases with increasing the temperature from 875 to 925 °C while the intensity of a set of diffraction lines at $2\theta = 44.8°$, 54.8° and 65.2° corresponding to a bcc structure (martensite) follows the reverse trend: the intensity increases as the temperature and/or time increases (Fig. 5B). The impoverishment in chromium and manganese of the alloy upper layers required for the formation of the oxide scale modifies the composition of the alloy resulting in the transformation of the metastable austenite phase in the thermodynamically stable martensite phase.

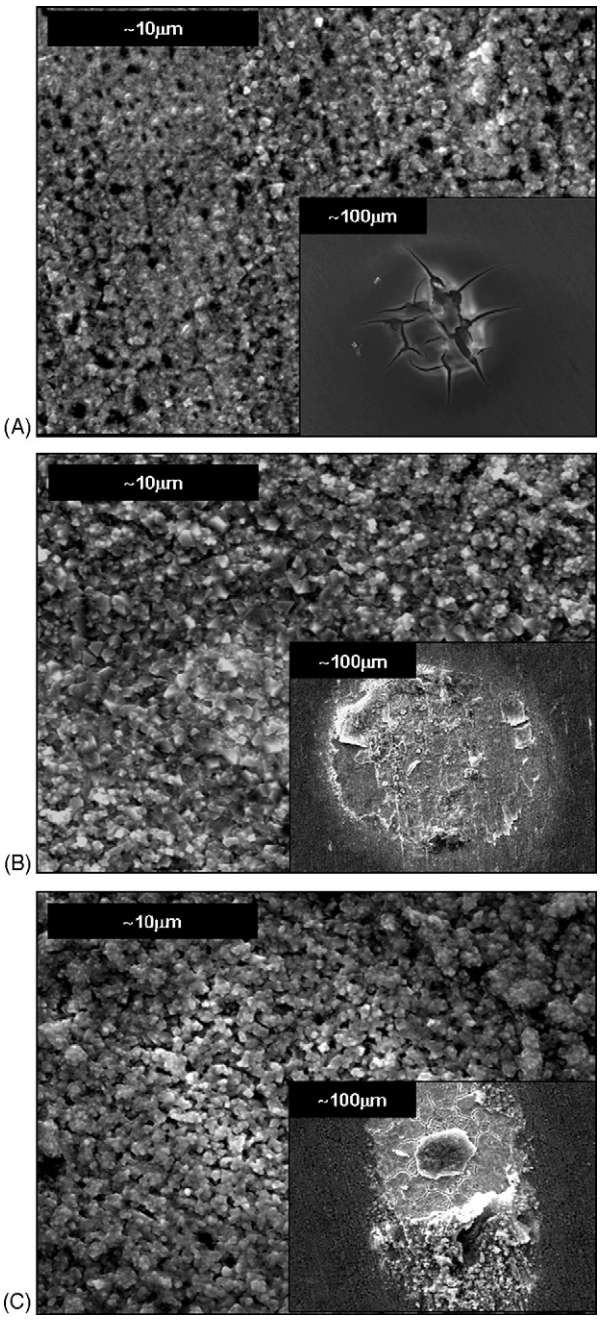

Fig. 4. SEM micrograph of the top view of AISI 304 austenitic stainless steel foil, treated at 900 °C for different time: (A) 30 min, (B) 90 min and (C) 120 min.

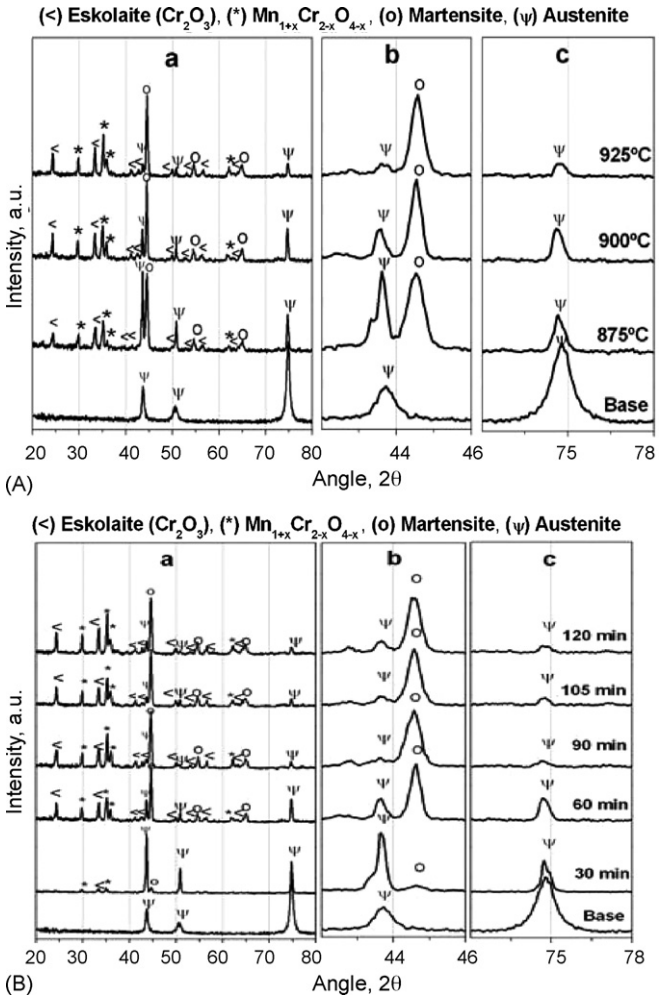

Fig. 5. XRD patterns of base alloy and monolith treated at different temperatures for 60 min (A) and different times at 900 °C (B).

The chemical compatibility of the catalytic layer with the metallic support depends on the chemical composition of the surface layer of the oxide scale. XPS measurements allow establishing the chemical composition of the uppermost layer of the oxide scale, as shown in Fig. 6. The high temperature oxidation results in Mn- and Cr-rich oxide scale with the atomic concentrations superiors to determined for the bare alloy. In addition to these elements, the presence of Fe and Si together with oxygen and the spurious carbon was always detected. While the oxidation state of the manganese cations is hardly determined by the shifts in the Mn(2p) level [9] the binding energy of the Cr(2p) peaks was associated to Cr^{3+} ions and the Fe (2p) level can be always fitted with a mixture of Fe^{2+} and Fe^{3+} ions. The concentration of manganese and chromium increases with the oxidation time while the concentration of iron and silicon decreases (Fig. 6B). These data are consistent with the short-circuit diffusion mechanism for the oxidation of the metallic alloy [16]. Moreover, the higher the oxidation temperature the higher the concentration of manganese and chromium in the oxide scale and the lower the concentration of iron and silicon are (Fig. 6A). The relative decrease observed in Fig. 6A for the highest temperature (925 °C) can be associated with the cracking and spalling of the oxide scale that occurs at this temperature leaving the metallic surface partially uncovered and hence increasing the relative amount of iron and silicon observed by the XPS analysis. The concentrations of Cr and Mn reach a maximum when the alloy is oxidized for 60 min at 900 °C, for higher temperatures cracking and spalling phenomena decrease the amount of these elements exposing the bare metal surface (Fig. 6A). If the oxidation temperature is kept constant at 900 °C a prolonged exposure does not result in an increase in Cr and Mn concentration which grows asymptotically above 60 min (Fig. 6B). The deviations from the smooth curve, observed in Fig. 6 are related to the cracking and spalling phenomena as described for prolonged oxidation times in Table 3 and Fig. 4.

A thick and homogeneous oxide scale containing Cr-Mn spinels and chromium oxides was obtained when the oxidation was performed at 900 °C for 60 min, and hence those conditions were selected for all the subsequent pre-treatments of the monoliths. XRD and XPS data provide limited information on the compositional and structural in-depth profile of the oxidized monoliths, to analyse in detail the depth profile of the elements forming the

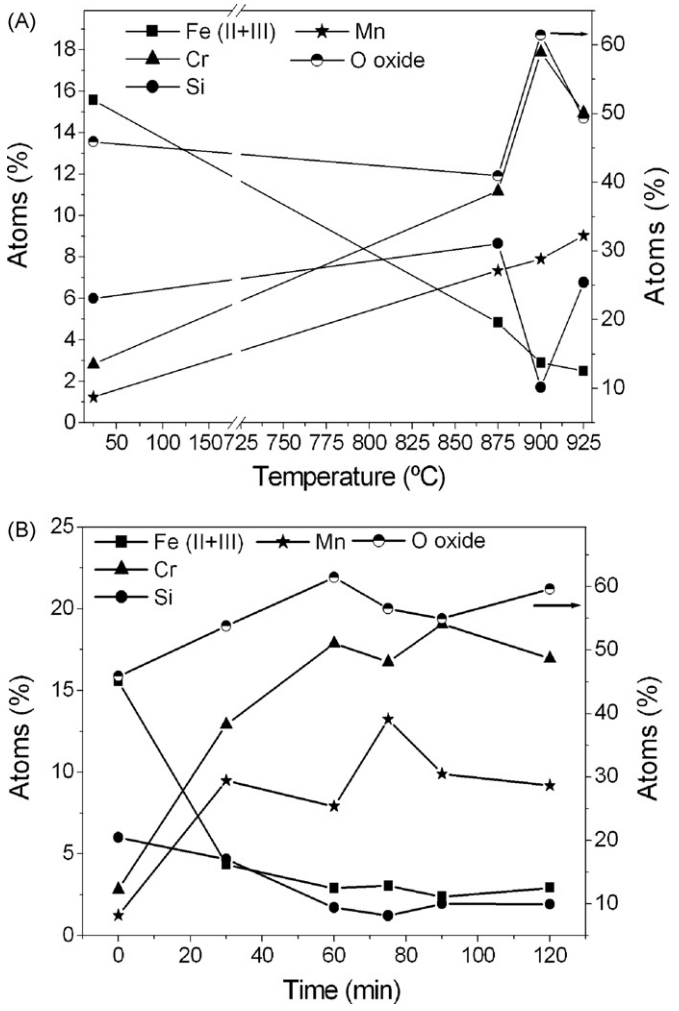

Fig. 6. Evolution of the steel surface composition with the pre-treatment temperature (A) and time (B).

oxide scale GD-OES experiments were carried out. For the sake of simplicity just the depth profile of the sample with the selected pre-treatment is shown, Fig. 7. From the GD-OES data it can be concluded that upon oxidation the surface and subsurface layers of the alloy are structured. The total scale thickness is measured to be 0.72 μm being composed of an outer layer 0.24 μm thick where Cr and Mn oxides are the dominant species. This layer according to XPS and XRD data must be formed by Cr-Mn spinels although the presence of iron ions substituting either Cr or Mn has to be taken into account for the outermost surface, as shown in Fig. 7. Underneath this layer, the oxide scale is composed almost exclusively of chromium oxides resulting in the α-Cr_2O_3 phase detected by XRD. At the scale–alloy interface a new phase develops mainly composed of silicon and oxygen. This phase must be of vitreous character since X-ray diffraction lines corresponding to silicon-containing phases are completely absent (Fig. 5). This Si-rich layer penetrates the alloy along grain boundaries [19,28].

3.2. Coating deposition

The roughness of the oxide scale generates a macroporous structure that facilitates the anchoring of the washcoat layer. Although the BET surface area of the oxidized monolith is not measurable, well below the limit of the ASAP 2020 apparatus. However, the SEM images demonstrate the existence of a macroporous structure together with a certain mesoporosity generated by the different crystals forming the scale. In Fig. 8, on a presented high-resolution top view SEM image of the generated oxide scale, pores within the oxide scale structure from the micron range to the nanometer range could be observed. In our case, the washcoating is carried out by filling the macroporous structure with the high surface area washcoat material, and by depositing the washcoat, as a layer, in the mesopores generated in the ceramic scale created upon oxidation of the metallic monolith. This later coating results in the strongest interaction between monolith and washcoat. The use of a colloidal CeO_2 dispersion favors this type of interaction. The combination of both procedures helps obtaining the desired amount of catalytic material deposited on the metallic monolith.

The effect of the solid concentration in the colloidal dispersion was studied in order to improve the uniformity of the CeO_2 layer. The amount of deposited CeO_2 was kept constant (ca. 100 mg) and therefore, the number of immersions for each concentration was adjusted (Table 4). Once the catalytic layer is deposited it can be either dried or dried and calcined prior to proceed to a new immersion. However, drying procedures in a ventilated oven at 120 °C results in a cracked catalytic layer, as shown in Fig. 9A. To avoid crack formation in the ceria coated layer during solvent removal (drying) several methods were tested. SEM images of the coated monolith with the commercial ceria colloid (20 wt.%) after solvent removal by various drying procedures are shown in Fig. 9. Drying procedures involving thermal treatment at 120 °C in static air result in a completely cracked coated layer that has even lost part of the coating

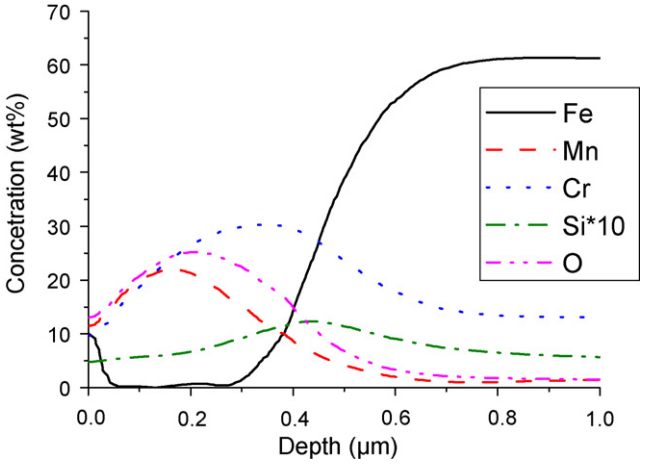

Fig. 7. GD-OES analysis of the oxide formed on AISI 304 oxidized at 900 °C for 60 min.

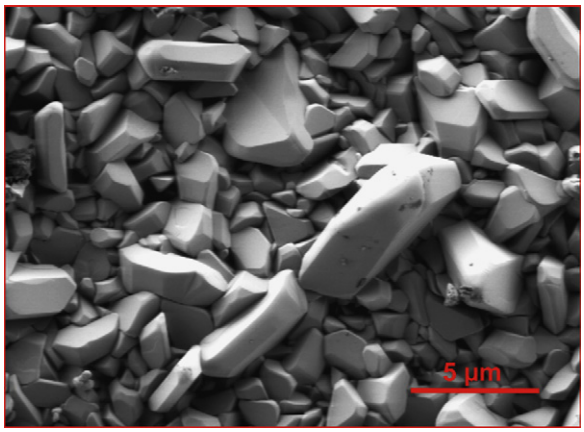

Fig. 8. High-resolution top view SEM image of the generated oxide scale at 900 °C for 60 min.

Table 4
Coated and number of layers with the variations on colloid concentration.

Concentration (wt.%)	No. of coatings	Loaded (mg)	Surface morphology (homogeneity)
20	1	95.0	Medium (Fig. 9a)
15	2	97.1	Medium (Fig. 10a)
10	3	97.0	Excellent (Fig. 10b)
5	5	101.0	Low (Fig. 10c)
2	5	90.0	Low (Fig. 10d)

upon drying (Fig. 9A). A procedure involving the drying and calcination in one step results in a uniform crack distribution (Fig. 9B). Upon drying the liquid will move from the wetter parts of the monolith to the drier parts as a result of capillary forces and as a consequence the oxide coating may agglomerate. In order to minimize these effects a freeze-drying procedure was set up (Fig. 9C and D). Freeze-drying works by freezing the material and then reducing the surrounding pressure and adding enough heat to allow the frozen water in the material to sublime directly from solid phase to gas. The freeze-drying for 2 h could results in incomplete solvent removal and the further elimination of the residual solvent provokes small cracks all over the coated layer. In this case a freeze-drying procedure lasting at least 4 h is required for ensuring a homogeneous coated, as shown in Fig. 9D. Vergunst et al. [29] observed that if the freeze-drying is stopped too early and is switched to the static drying procedure, a new evaporation front arises, which attracts the liquid from inside the front, shown a heterogeneous coated.

The preparation of the catalyst is obtained by a sequence of immersions and freeze-drying procedures whose number depends on the amount of catalyst desired and the solid concentration of colloidal dispersion. Table 4 presents the data obtained for different solid concentrations ranging from 2 to 20 wt.% dried by freeze-drying. As it should be expected on decreasing the solid concentration the number of immersions must be increased. However, to get a thick and homogeneous layer a compromise between the solid concentration and the number of immersions should be reached. If the solid concentration is too low the coating layer cracks and shows poor adherence (Fig. 10C and D), but if it is too high the coating layer is not homogeneous presenting areas with the agglomerated material (Fig. 10A). A compromise is obtained when using a ceria colloidal dispersion containing 10 wt.% of solids. After three deposited catalytic layers a thick coating layer containing ca. 100 mg catalyst with a good homogeneity, where the cracks are completely eliminated, is obtained. Moreover, this coating procedure results in an excellent adherence of the coating. After the ultrasonic test used for determining the adherence of the coating only ≈1.0 wt.% of the layer was lost. The N_2 adsorption–desorption isotherm of the whole monolith shows the presence of mesoporosity and a H2 hysteresis loop is observed. The adsorption isotherm of the coated monolith corresponds to type IV isotherm according to the IUPAC classification, which is typical for mesoporous materials. The BET surface area of the monolith is 10 m^2, with an average pore diameter according to the BJH method of 4.1 nm. These values are consistent with those for the ceria powder obtained by freeze-drying and further calcination of colloidal dispersion with specific surface of 100 $m^2\,g^{-1}$ and similar average pore size.

The homogeneous and adherent ceria layer on the monolith has a thickness of ca. 1 μm as determined by GD-OES

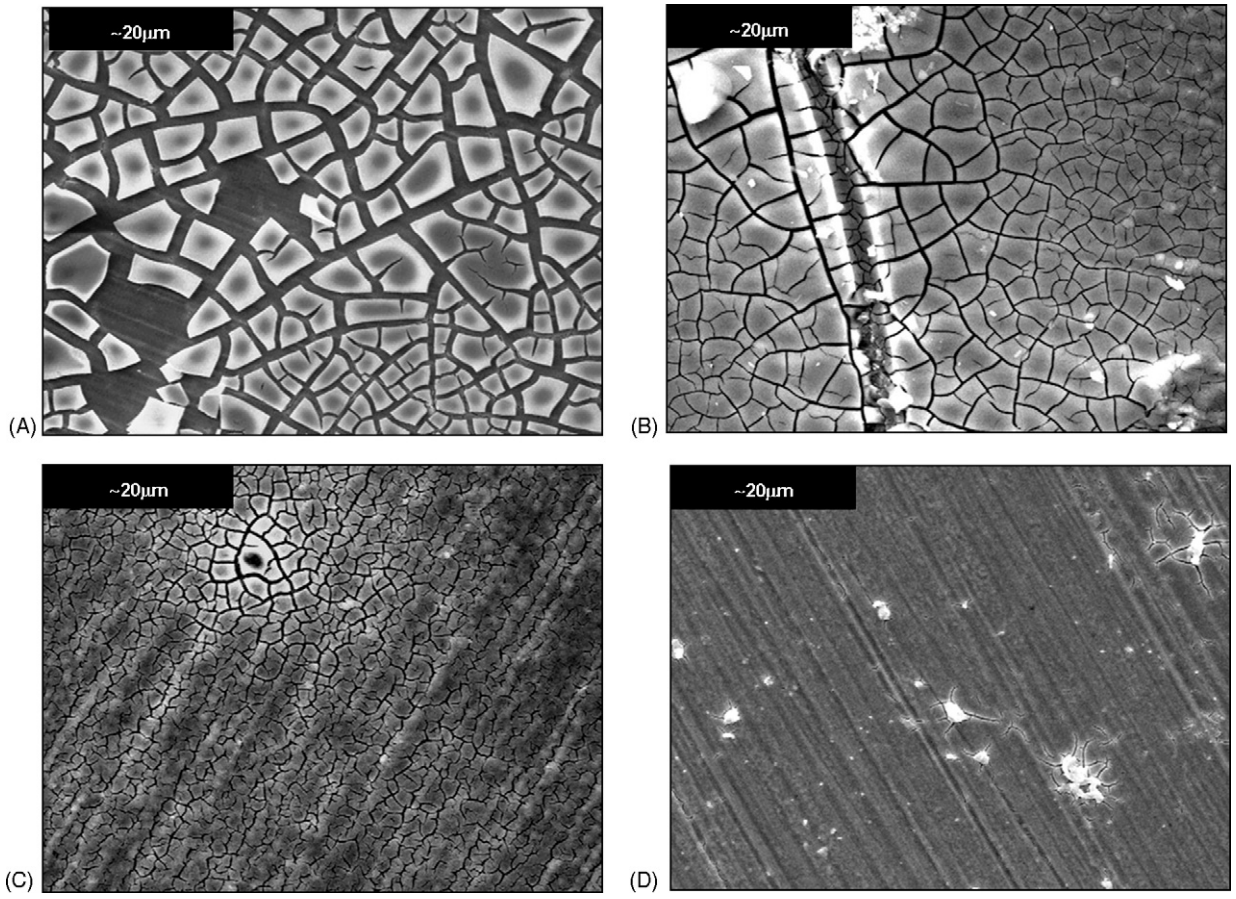

Fig. 9. SEM micrograph. Top view of different monolith with ceria layer. Effect of the drying method. (A) Flash dried, (B) dried and calcined in one step, freeze-drying (C) 2 h and (D) 4 h and then calcined.

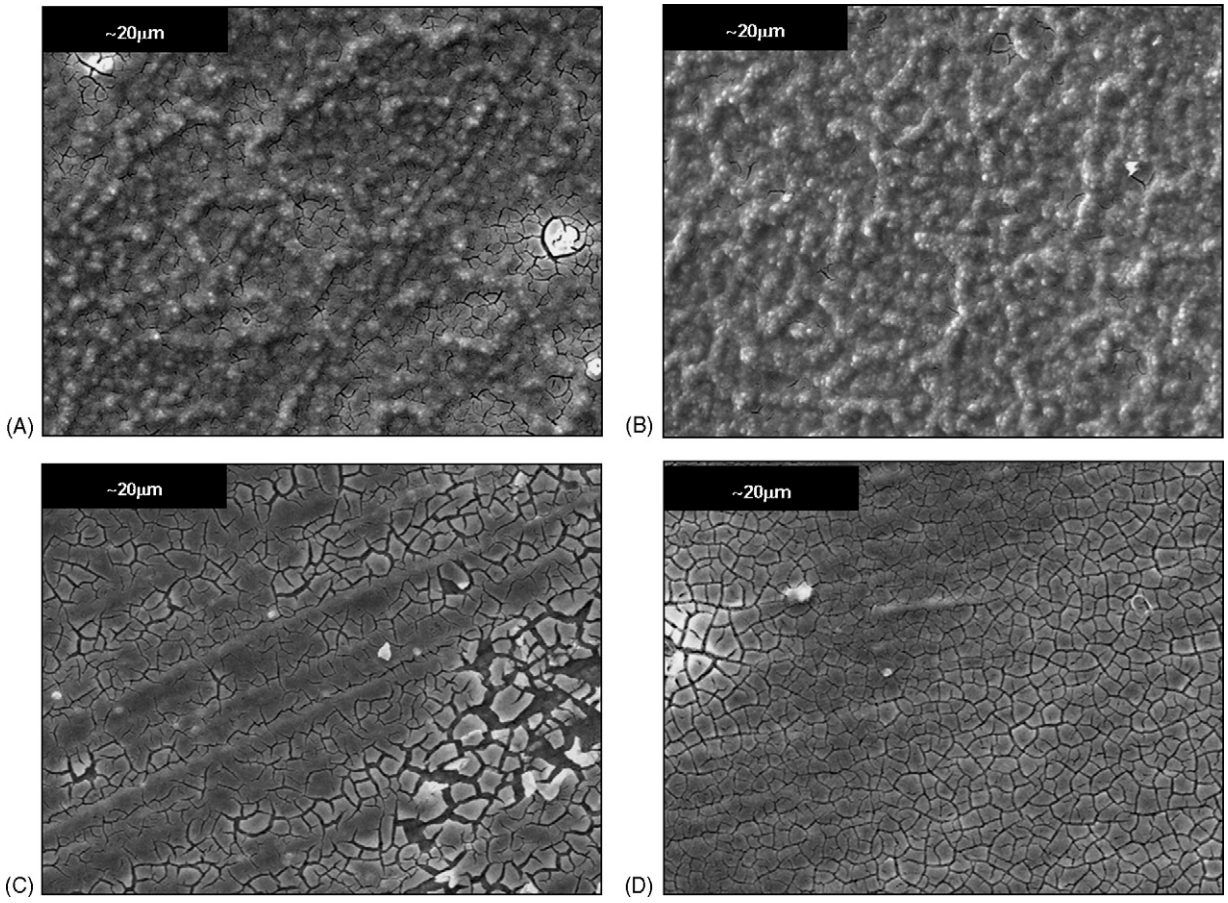

Fig. 10. SEM micrograph. Top view of different monolith with ceria layer. Effect of the multiple depositions with different colloid concentrations. (A) 15% twice, (B) 10% three time, (C) 5% five times and (D) 2% five times.

(Fig. 11). This thickness value is consistent with the catalyst loading (0.425 mg cm^{-2}) and presents an apparent density at around 65% of the ideal ceria density (7.3 g cm^{-3}). The coating procedure results in a modification of the oxide scale formed upon oxidation, chromium and manganese diffuse to the external surface during the coating procedure forming an outer layer of ca. 0.60 μm on top of the inner chromia layer. Together with this a surface enrichment in silicon is observed as well as a migration of the ceria to the alloy–scale interface. The migration of lanthanide elements to this interface results in an improved adherence and high temperature oxidation resistance [20,21,23,28].

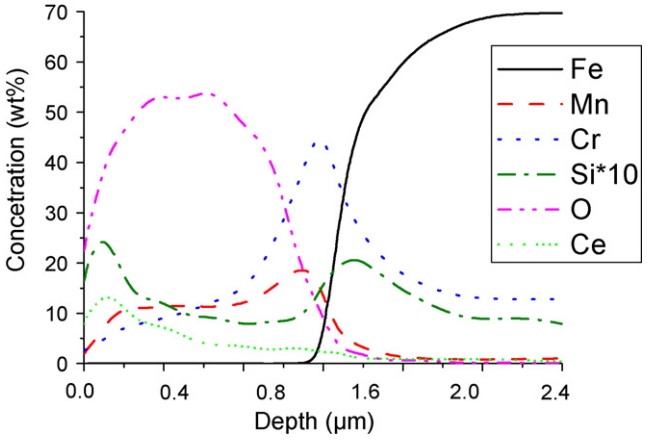

Fig. 11. GD-OES analysis of the oxidized AISI 304 with ceria coating.

3.3. Au deposition

Gold was deposited via ion exchange using gold acetate. Gold acetate is used in order to prevent pitting corrosion phenomena on the metallic substrate [13,14,30]. In water solution a series of gold (III) complexes where the acetate groups are partially replaced by hydroxyl groups are formed depending their relative proportion of the acetate concentration and pH, Eq. (1) [31]. The CeO_2-coated monoliths were immersed in 25 ml of an aqueous solution containing 40 ppm of $Au(CH_3COO)_3$ and kept in this solution for either 30 or 90 min in order to study the effect of the contact time on the homogeneity and gold loading on the ceria layer. After withdrawing the monoliths from the solution at 3 cm h^{-1}, they were calcined in air with a temperature ramp of 2 °C min^{-1} up to 500 °C for 4 h,

$$Au(CH_3COO)_3 + H_2O \rightarrow Au(CH_3COO)_{3-n}(OH)_n(H_2O)_p \quad (1)$$

The support is in contact with a solution containing either positively or negatively charged complexes depending on the pH and acetate concentration. As these complexes react with surface hydroxyl groups of the ceria layer the pH of the solution is modified as well as the acetate concentration, in this way the ion exchange rate is modified and the amount of loaded gold may change. The ICP-OES measurements of the exchanged catalysts resulted in a gold loading of 0.9 wt.% and 0.2 wt.%, after 30 min and 90 min immersion time, respectively. SEM micrographs of the catalytic layer after gold loading are shown in Fig. 12. The homogeneity of the ceria layer is apparently preserved after 30 min immersion in the gold solution, and the presence of some small gold clusters is evident on the monoliths (Fig. 12A). However, after 90 min of immersion in the gold-containing solution SEM images show that the catalytic layer is

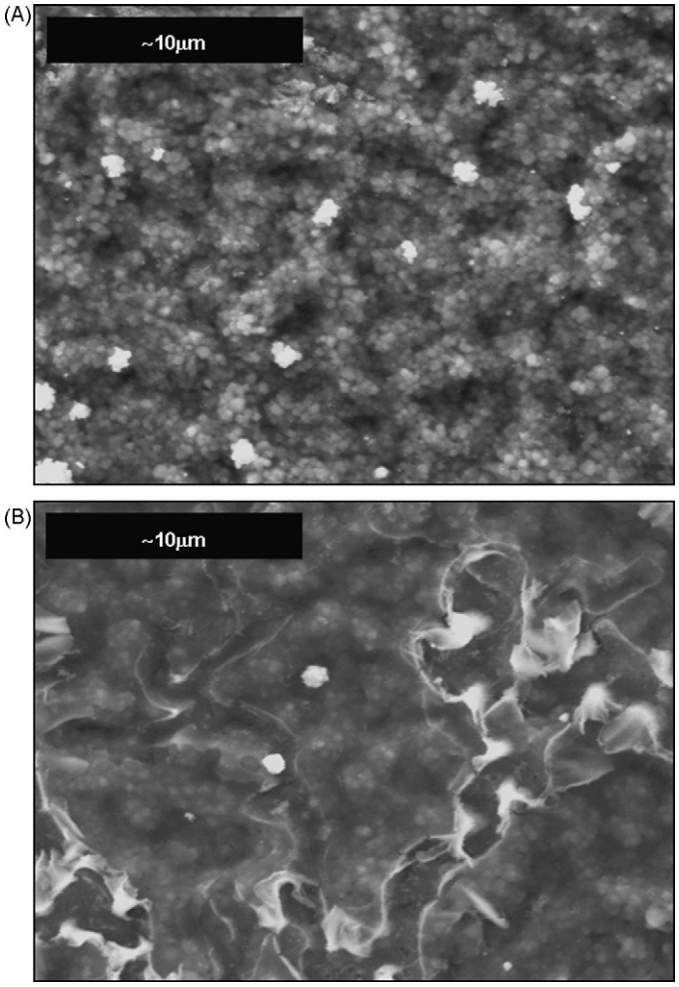

Fig. 12. SEM micrograph. Top view of different monolith with Au/ceria layer. Effect of the immersion time. (A) 30 min and (B) 90 min.

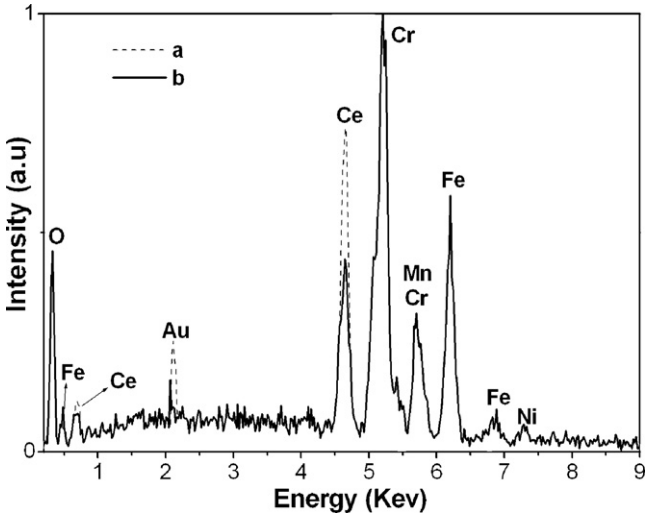

Fig. 13. EDX microanalysis for monolith with Au/ceria layer. Effect of the immersion time. (a) 30 min and (b) 90 min.

not longer homogeneous (Fig. 12B). Whatever the immersion time the BET surface area of the monoliths decrease with respect to the CeO_2-coated layer from 10 to 4 and 3 m^2/monolith after 30 and 90 min immersion, respectively. The adherence of the coating significantly diminishes after gold deposition, 2.0 wt.% and 3.0 wt.% of the layer was lost after the ultrasonic test for 30 and 90 min immersion, respectively. The presence of gold, confirmed by EDX microanalysis (Fig. 13), alters the adherence of the ceria layer and probably decreases the amount of loaded ceria justifying the decrease of BET surface area. In addition, the presence of metallic cations that may undergo redox processes would affect the ion exchange process with the gold complexes. Those results demonstrate that the contact time with the metallic solutions is crucial in order to preserve the homogeneity of the ceramic layer and to avoid gold clustering.

3.4. Catalytic oxidation test

The oxidation of CO is used to test the prepared catalytic devices. Fig. 14 presents CO ignition curves for the pre-treated AISI 304 steel monoliths coated with the CeO_2 support and the Au-CeO_2 catalyst. The pre-treated AISI 304 steel monolith was not active for the oxidation of CO at temperatures below 300 °C. The CO conversion started at 400 °C reaching less than 5% conversion at 500 °C. When the monoliths are coated with CeO_2 the CO conversion is greatly enhanced (Fig. 12A). The redox properties of CeO_2, resulting in the capacity to accommodate variable amounts of oxygen vacancies either in the bulk or the surface, has been proved to increase the catalytic activity in the CO and VOCs oxidation reactions [32–34]. Gold clearly enhances the catalyst activity (Fig. 12A) achieving a complete conversion of CO at temperatures close to 250 and 120 °C for the monoliths containing 0.2 and 0.9 wt.% Au, respectively. The activity increases with increasing the Au loading as previously reported for most gold systems [35,36] since the catalytic activity is related to the number of active sites. On adding water to the reaction system, the ignition curves move towards the left, lower temperatures (Fig. 12B). Water exerts a clear influence in the redox reactions involved in the catalytic oxidation of CO since

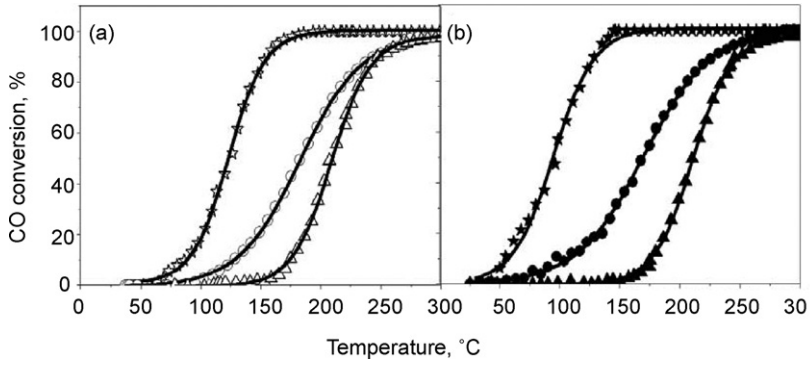

Fig. 14. Catalytic oxidation of CO (a) without water and (b) with water using pre-treated metallic monoliths coated by Au/CeO_2. Symbols (△ and ▲) with CeO_2 and immerses into gold acetate solutions (☆ and ⋆) 30 min and (◯ and ●) 90 min.

it has been demonstrated that favors the redox reactions involving Au nanoparticles and oxygen vacancies resulting in the redispersion of the gold clusters during reaction and, on the other hand, water competes with gold nanoparticles for surface oxygen vacancies that are required for nucleating gold species [32,35,37].

4. Conclusions

When using AISI 304 stainless steel as a substrate for catalytic purposes it is necessary to generate an oxide scale strongly adherent to the base alloy, highly homogeneous and rough in order to ensure a good adherence of the catalysts. In this study it has been shown that the morphology, integrity and homogeneity of the scale are strongly influenced by temperature and time of the treatment. Under mild conditions (900 °C, synthetic air) an oxide layer composed mainly of manganese and chromium oxides is developed ($Mn_{1+x}Cr_{2-x}O_{4-x}$, Cr_2O_3). Optimized physical parameters (roughness, homogeneity, and adherence) are obtained when the oxide layer is generated in synthetic air at 900 °C for 60 min. The drying procedure turned out to be the most critical variable for the adherence and homogeneity of the catalytic ceria layer, while the ceria colloid concentrations in the starting aqueous dispersion seems to have only a threshold effect. The monolithic reactors prepared this way containing Au/CeO_2 layers are active in the oxidation of CO.

Acknowledgments

Financial support by Spanish Ministerio de Ciencia y Tecnología - MCYT (MAT2006-06540-C02), CYTED Programme (PI0269), Programme Alβan-European Union Programme of High Level Scholarships for Latin America (L.M. Martínez T Ph.D. UE E04D046878CO Scholarship) and Juan Almagro (ACERINOX S.A. Spain) for his help with high-resolution SEM experiments.

References

[1] A. Cybulski, J.A. Moulijn, Catal. Rev. Sci. Eng. 36 (1994) 179.
[2] M.F.M. Zwinkels, S.G. Järas, P.G. Menon, Stud. Surf. Sci. Catal. 91 (1995) 85.
[3] N. Burgos, M. Paulis, J. Sambeth, J.A. Odriozola, M. Montes, Stud. Surf. Sci. Catal. 118 (1998) 157.
[4] R.M. Heck, S. Gulati, R.J. Farrauto, Chem. Eng. Sci. 82 (2001) 149.
[5] T.A. Nijhuis, M.T. Kreutzer, A.C.J. Romijn, F. Kapteijn, J.A. Moulijn, Chem. Eng. Sci. 56 (2001) 823.
[6] J.P. Reymond, Catal. Today 69 (2001) 343.
[7] N. Burgos, M. Paulis, M.M. Antxustegi, M. Montes, Appl. Catal. B 38 (2002) 251–258.
[8] N. Burgos, M. Paulis, M. Montes, J. Mater. Chem. 13 (2003) 1458–1467.
[9] I. Barrio, I. Legorburu, M. Montes, M.I. Dominguez, M.A. Centeno, J.A. Odriozola, Catal. Lett. 101 (2005) 151.
[10] P. Avila, M. Montes, E.E. Miro, Chem. Eng. J. 109 (2005) 11.
[11] M.I. Dominguez, M. Sanchez, M.A. Centeno, M. Montes, J.A. Odriozola, Appl. Catal. A 302 (2006) 96–103.
[12] D.M. Frias, S. Nousir, I. Barrio, M. Montes, L.M. Martinez T, M.A. Centeno, J.A. Odriozola, Appl. Catal. A 325 (2007) 205.
[13] M.I. Dominguez, M. Sanchez, M.A. Centeno, M. Montes, J.A. Odriozola, J. Mol. Catal. A 277 (2007) 145.
[14] L.M. Martinez T, D.M. Frias, M.A. Centeno, A. Paul, M. Montes, J.A. Odriozola, Chem. Eng. J. 136 (2008) 390.
[15] O. Sanz, L.C. Almeida, J.M. Zamaro, M.A. Ulla, E.E. Miro, M. Montes, Appl. Catal. B 78 (2008) 166.
[16] M. Schütze, in: M. Schütze (Ed.), Corrosion and Environmental Degradation, vol. I, Wiley-VCH, Weinheim, 2000.
[17] J. Stringer, Mater. Sci. Eng. A 120 (1989) 129.
[18] B-H.E. Evans, Mater. Sci. Eng. A 120 (1989) 139.
[19] A. Paúl, R. Sánchez, O.M. Montes, J.A. Odriozola, Oxid. Met. 67 (2007) 87.
[20] M.J. Capitan, A. Paul, J.L. Pastol, J.A. Odriozola, Oxid. Met. 52 (1999) 447.
[21] A. Paúl, S. Elmrabet, F.J. Ager, J.A. Odriozola, Surf. Int. Anal. 30 (2000) 176.
[22] A. Paúl, J.A. Odriozola, Mater. Sci. Eng. A 300 (2001) 22.
[23] A. Paúl, S. Elmrabet, F.J. Ager, J.A. Odriozola, M.A. Respaldiza, M.F. da Silva, J.C. Soares, Oxid. Met. 57 (2002) 33.
[24] B.L. Yang, F.P. Daly, J.M. Watson, T. Manzanec, S.P. Fitzgerald, B.R. Johnson, X. Li, Ch. Cao, Y.-H- Chin, A.L. Tonkovich, R. Arora, D.J. Hesse, D. Qiu, R. Taha, J.J. Ramler, Y. Wang, US Patent 2005/0271563 A1 (2005).
[25] I.M. Wolff, L.E. Iorio, T. Rumpf, P.V.T. Scheers, J.H. Potgieter, Mater. Sci. Eng. A 241 (1998) 264.
[26] S. Yasaki, Y. Yoshino, K. Ohkubo, US Patent 5,208,206 (1993).
[27] S. Osgerby, K. Berriche-Bouhanek, H.E. Evans, Mater. Sci. Eng. A 412 (2005) 182.
[28] A. Paúl, S. Elmrabet, J.A. Odriozola, Mater. Sci. Forum 383 (2002) 125.
[29] T. Vergunst, F. Kapteijn, J.A. Moulijn, Appl. Catal. A 213 (2001) 179.
[30] F. Romero-Sarria, L.M. Martinez T, M.A. Centeno, J.A. Odriozola, J. Phys. Chem. C 111 (2007) 14469.
[31] L.F. Warren Jr., P.H. Cunningham, US Patent 4,933,204 (1990).
[32] A. Trovarelli, Catal. Rev. Sci. Eng. 38 (1996) 439.
[33] C. Agrafiotis, A. Tsetsekou, C.J. Stournaras, A. Julbe, L. Dalmazio, C. Guizard, J. Eur. Ceram. Soc. 22 (2002) 15.
[34] M.A. Centeno, M. Paulis, M. Montes, J.A. Odriozola, Appl. Catal. A 234 (2002) 65.
[35] M.A. Centeno, C. Portales, I. Carrizosa, J.A. Odriozola, Catal. Lett. 3–4 (2005) 289.
[36] S. Ivanova, V. Pitchon, Y. Zimmermann, C. Petit, Appl. Catal. A 298 (2006) 57.
[37] C. Padeste, N. Cant, D. Trimm, Catal. Lett. 18 (1993) 305.